Yellow-Emitting, Pseudo-Octahedral Zinc Complexes of Benzannulated N^N^O Pincer-Type Ligands

Issiah B. Lozada,[a] Jason D. Braun,[a] J. A. Gareth Williams,[b] David E. Herbert[a]**

[a] Department of Chemistry and the Manitoba Institute for Materials, University of Manitoba, 144 Dysart Road, Winnipeg, Manitoba, R3T 2N2, Canada; *david.herbert@umanitoba.ca

[b] Department of Chemistry, Durham University, Durham, DH1 3LE, UK;
*j.a.g.williams@durham.ac.uk

ABSTRACT

A series of yellow-emitting, pseudo-octahedral Zn(II) complexes supported by monoanionic, tridentate acetylacetone-derived N^N^{-}^O ligands incorporating phenanthridine (benzo[*c*]quinoline) units is presented. These species emit weakly in solution but exhibit extended millisecond luminescence lifetimes in the solid state at room temperature, and in a frozen glass at 77 K, indicative of phosphorescence from low-lying triplet excited states. Excitation spectra indicate a role for aggregation in enhancing emission in the solid state. In contrast to four-coordinate phenanthridinyl amide-supported tetradentate Zn(II) complexes which are non-emissive in fluid solution, solid-state X-ray crystallographic structures, solution IR spectroscopy and computational analysis all indicate delocalized character for the central deprotonated NH which tempers the amido character of the ligand. This design provides a mechanism for ‘turning on’ long-lived luminescence from *N*-heterocycle/amido-supported Zn(II) coordination compounds.

Introduction

Photoactive and luminescent complexes of abundant metals are increasingly sought as cost-effective and sustainable components of light-emitting devices (LEDs), sensors and photocatalysts.[1,2] Zinc is more abundant than copper in the Earth's crust and is accordingly an attractive target in these areas.[3] While not usually strongly emissive in fluid solution,[4–7] Zn(II) complexes are receiving growing attention for use in the emissive layer of LEDs, similar to the application of aluminum *tris*(8-hydroxyquinoline).[8,9] Among the solid-state Zn(II) emitters reported, those displaying yellow emission (550-580 nm) are rare. Examples of yellow-green emitting complexes include a series with Schiff base ligands that incorporate pendant diphenylamino groups ($\lambda_{\text{em, max}}$ = 544 nm, ϕ = 20.9%; powder).[10] These complexes exemplify the typical coordination environment of emissive Zn(II) fluorophores: four-coordinate, pseudo-tetrahedral geometry via hard, monoanionic, N^O-binding, bidentate ligands.[11]

Many six-coordinate Zn(II) complexes are also known, particularly when the ligands are not sterically encumbered. Multidentate ligands, in particular, favor the formation of higher coordination numbers,[12–17] as do intramolecular interactions (for example, between ligands[18]). Five-coordinate complexes of the form (N^N^N)$ZnCl_2$ can be formed using diimino-pyridine ligands,[19] while six-coordinate zinc porphyrins[20] have been used to construct three-dimensional coordination polymer networks[21] and in the template-directed synthesis of nano-sized rings.[22] Luminescent, six-coordinate Zn(II) complexes featuring two tridentate, N^N^O-chelating, oxime/hydrazone ligands have also been reported.[23] Meanwhile, dinuclear Zn_2 clusters with 5-coordinate metal ions have been reported that luminesce strongly with a quantum yield of 93% (72% in the solid-state, λ_{max} = 537 nm).[7] Less typical of Zn(II) complexes are those that exhibit detectable phosphorescence, either as solids or in fluid solution, owing to the smaller spin-orbit coupling (SOC) constants of the 3*d* transition metals compared to 4*d* and 5*d* metals; the higher SOC associated with the heavier metals facilitates efficient intersystem crossing (ISC) to triplet state manifolds and subsequent radiative decay from the T_1 state. Emissive zinc complexes are thus usually fluorescent, rather than phosphorescent, with lifetimes in the nanosecond regime. Phosphorescence with zinc is often limited to complexes with ligated heavy halides (thanks to the external heavy atom effect),[24,25] clusters, or metal-organic frameworks.[26–28]

We have been developing multidentate ligand scaffolds containing benzannulated *N*-heterocyclic donor arms, in particular ones that incorporate phenanthridine (3,4-benzoquinoline).[29,30] Bidentate phenanthridine-containing P^N ligands can be used to construct both binuclear[31] and mononuclear[32] Cu(I) solid-state emitters, while monoanionic, tridentate N^N⁻^N pincer-type ligands enable the formation of deep-red emitting Pt(II) phosphors[33,34] and Fe(II) complexes with unique photophysical properties.[35] Related N^N^O ligand variants can be formed too, by condensation of aminophenanthridines with acetylacetone, and they may be used as multidentate, benzannulated ligand scaffolds.[36,37] Here, we demonstrate the utility of such ligand architectures in producing six-coordinate, pseudo-octahedral Zn(II) complexes which exhibit very long-lived, moderately intense solid-state emission in the yellow-green region of the electromagnetic spectrum. A potential mechanism to ‘turn-on’ phosphorescence is proposed based on density functional theory (DFT) and time-dependent DFT (TDDFT) calculations.

Results and Discussion

The N^N(H)^O proligands $^{\mathbf{R}}\mathbf{LH}$ (R = Me, *t*Bu, CF_3) were isolated following our previously reported protocol that utilizes the acid-catalyzed condensation of 4-aminophenanthridine with acetylacetone.[36,38] Zinc complexes of these ligands, $Zn(^{\mathbf{R}}\mathbf{L})_2$, were prepared in a similar way to homoleptic Zn(II) species supported by monoanionic, bidentate *N*-phenyl-4-aminophenanthridines.[39] That is, via the dropwise addition of a solution of diethylzinc in hexanes into a solution of the proligands in 3:1 hexanes/toluene, both pre-cooled to -38 °C, which is then warmed to ambient temperature (Scheme 1a). Solutions of the proligands in the binary solvent mixture were pale yellow but grew more intensely colored on addition of diethylzinc, and bright yellow precipitates formed after stirring overnight. These solids were isolated by filtration and purified by repeated washing with cyclohexane or recrystallization from hot cyclohexane. Zn($^{\mathbf{R}}\mathbf{L}$)$_2$ complexes were isolated in this way in yields of 54, 84 and 79% for R = *t*Bu, Me and CF_3, respectively. The increased solubility of Zn($^{\boldsymbol{t}\mathbf{Bu}}\mathbf{L}$)$_2$ in organic solvents conferred by the *tert*-butyl substituents likely contributes to the reduced isolated yield. In contrast to four-coordinate, homoleptic, *bis*[phenanthridinyl-4-(*N*-phenyl)amido]zinc(II),[39] Zn($^{\mathbf{R}}\mathbf{L}$)$_2$ are all stable to both air and ambient moisture, as well as to mildly acidic solvents such as chloroform. Only one set of ^{1}H and ^{13}C NMR signals is observed in solution, suggesting that the two ligands have the same magnetic environment in solution which proffers C_2 symmetry to the complexes. In the ^{1}H NMR spectrum, coordination to Zn(II) induces a ~0.7 ppm shift to lower frequency of the N=C$_6$*H* resonance of the phenanthridinyl ligand arms [e.g., δ(N=C$_6$*H*): $^{\mathbf{Me}}\mathbf{LH}$, 9.29 ppm; Zn($^{\mathbf{Me}}\mathbf{L}$)$_2$, 8.58 ppm] which likely results from ring-current induced shielding by the (N^O)Zn chelate.[38]

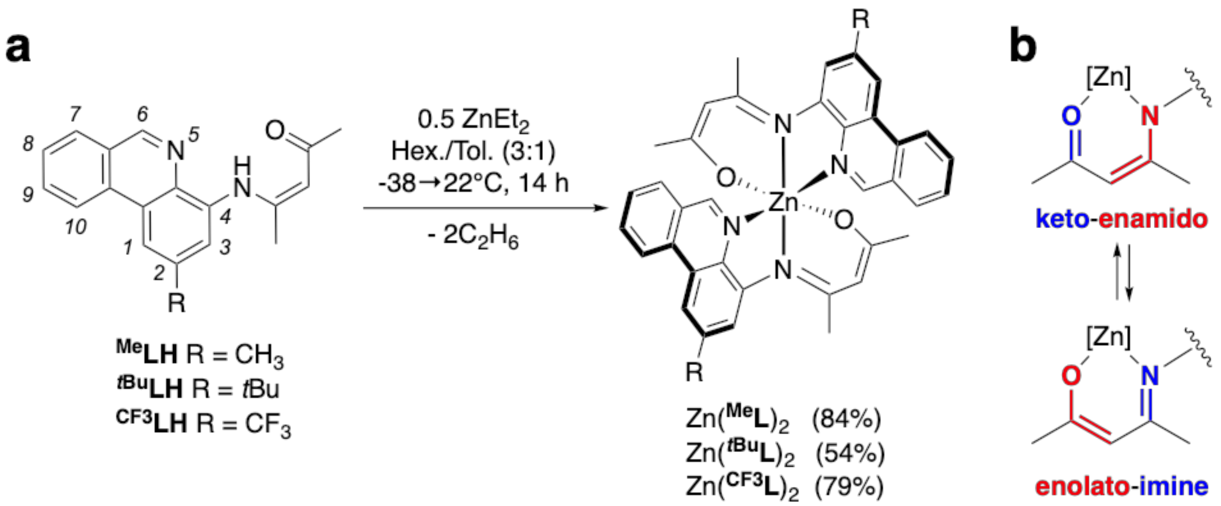

Scheme 1. (a) Synthesis of Zn($^{\mathrm{R}}$**L**)$_2$ with isolated yields indicated in parentheses. The IUPAC numbering scheme for phenanthridines is shown in italics for $^{\mathrm{R}}$**LH**. (b) Canonical forms of the tautomers possible for $^{\mathrm{R}}$**L**.

The solid-state structures of Zn($^{t\mathrm{Bu}}$**L**)$_2$ and Zn($^{\mathrm{CF3}}$**L**)$_2$ determined using single-crystal X-ray diffraction confirm the pseudo-octahedral coordination around the metal center (Figure 1). The structure of Zn($^{t\mathrm{Bu}}$**L**)$_2$ contains crystallographically distinct ligand environments, while Zn($^{\mathrm{CF3}}$**L**)$_2$ possesses the same approximate C_2 point group symmetry observed in solution by NMR spectroscopy. The asymmetry of Zn($^{t\mathrm{Bu}}$**L**)$_2$ in the solid state appears to arise from the presence of short-contact, non-covalent $\mathrm{C{-}H}^{\mathrm{phenanthridinyl}}\cdots\pi^{\mathrm{phenanthridinyl}}$ interactions between adjacent Zn(II) complexes, and non-bonding interactions between a C*H* unit of co-crystallized CH_2Cl_2 and the oxygen donor and $\pi_{\mathrm{C=N}}$ of the ketoiminate chelate ring (Figure S1). Indeed, the optimized geometry of Zn($^{t\mathrm{Bu}}$**L**)$_2$ in the gas phase (*vide infra*) presents a quite symmetric environment around the metal. Chelating ligands of the $^{\mathrm{R}}$**L** type can exist in tautomeric forms with anionic character localized at either nitrogen ('amido') or oxygen ('alkoxy'; Scheme 1b). The Zn1–O1/2 (2.060-2.075 Å) and Zn1-N2/4 (2.112-2.131 Å) bond distances suggest that a metal-alkoxy descriptor is more appropriate here. In general, in Pt(II) and boron complexes of $^{\mathbf{R}}\mathbf{L}$, the enolato-imine tautomer predominates upon deprotonation or coordination to metal centres,[36–38] while structural and spectroscopic data for the proligands ($^{\mathbf{R}}\mathbf{LH}$) are more consistent with the keto-enamine tautomer[36] [C15–N2 / C17–O1: $^{t\mathbf{Bu}}\mathbf{LH}$, 1.363(3) / 1.244(3) Å;[36] Zn($^{t\mathbf{Bu}}\mathbf{L}$)$_2$, 1.315(11) / 1.255(10) Å; Zn($^{\mathbf{CF3}}\mathbf{L}$)$_2$, 1.328(3) / 1.263(3) Å].

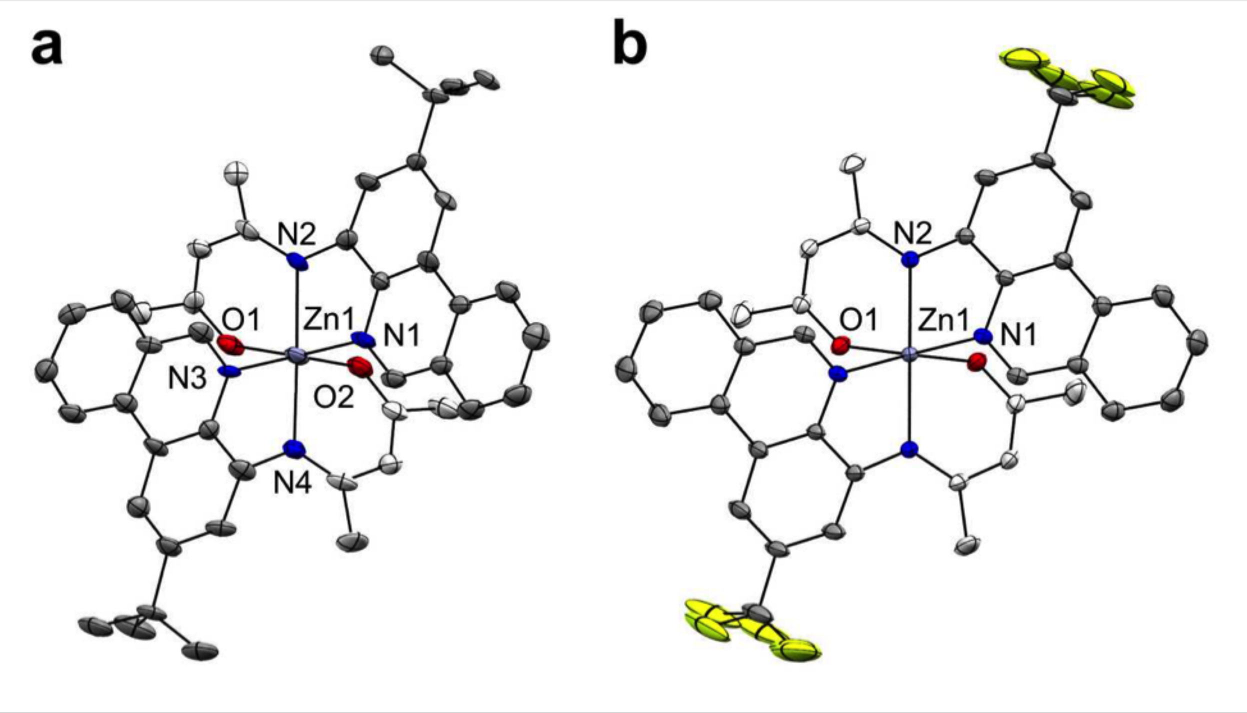

Figure 1. Solid-state structures of (a) Zn($^{t\mathbf{Bu}}\mathbf{L}$)$_2$ and (b) Zn($^{\mathbf{CF3}}\mathbf{L}$)$_2$ with thermal ellipsoids shown at 50% probability levels. Hydrogen and co-crystallized solvents are omitted for clarity. Selected bond lengths (Å) and bond angles (°) for Zn($^{t\mathbf{Bu}}\mathbf{L}$)$_2$: Zn1–N1 2.201(8), Zn1–N3 2.188(7), Zn1–N2 2.112(6), Zn1–N4 2.131(6), Zn1–O1 2.060(6), Zn1–O2 2.066(6); N1–Zn1–N3 89.8(3), N2–Zn1–N4 168.6(3), O1–Zn1–O2 91.7(2), N1–Zn1–N2 75.7(3), N1–Zn1–N4 95.2(3), N1–Zn1–O1 163.7(2), N1–Zn1–O2 90.1(2), N2–Zn1–N3 96.5(2), N3–Zn1–N4 76.2(3), N3–Zn1–O1 93.0(3), N3–Zn1–O2 163.5(2). Zn($^{\mathbf{CF3}}\mathbf{L}$)$_2$: Zn1–N1 2.203(2), Zn1–N2 2.103(2),

Zn1–O1 2.075(2); N1–Zn1–N1 97.49(12), N1–Zn1–N2 76.42(8)/98.44(8), O1–Zn1–O1 93.81(12), N1–Zn1–O1 86.51(8)/164.12(8).

Infrared (IR) spectra of the complexes in the solid state were collected to further examine the tautomerism, and gas-phase IR spectra simulated from their respective optimized geometries (Figure S2-S4). The proligands are generally characterized by two relevant vibrational modes: $\nu_{\mathrm{C=O,stretch}}$ ($^{\mathbf{Me}}\mathbf{LH}$/$^{\boldsymbol{t}\mathbf{Bu}}\mathbf{LH}$, 1617 cm^{-1}; $^{\mathbf{CF_3}}\mathbf{LH}$, 1634 cm^{-1}) and $\nu_{\mathrm{N\text{-}H,bend}}$ ($^{\mathbf{Me}}\mathbf{LH}$, 1569 cm^{-1}; $^{\boldsymbol{t}\mathbf{Bu}}\mathbf{LH}$, 1570 cm^{-1}; $^{\mathbf{CF_3}}\mathbf{LH}$, 1579 cm^{-1}). Upon deprotonation and coordination to zinc, the characteristic $^{\mathbf{R}}\mathbf{LH}$ IR frequencies are replaced by new bands which appear between 1400 and 1600 cm^{-1}. DFT suggests that two vibrational modes (insets, Figure S2-S4) dominate this region, in addition to lower intensity vibrational modes of similar character. The more intense, lower energy peak [Zn($^{\mathbf{Me}}\mathbf{L}$)$_2$ 1391 cm^{-1}; Zn($^{\boldsymbol{t}\mathbf{Bu}}\mathbf{L}$)$_2$ 1396 cm^{-1}; Zn($^{\mathbf{CF_3}}\mathbf{L}$)$_2$ 1380 cm^{-1}] is characterized by co-stretching of the C–N and C–O subunits of the enolato-imine fragment. The appearance of a higher energy peak [Zn($^{\mathbf{Me}}\mathbf{L}$)$_2$ 1449 cm^{-1}; Zn($^{\boldsymbol{t}\mathbf{Bu}}\mathbf{L}$)$_2$ 1453 cm^{-1}; Zn($^{\mathbf{CF_3}}\mathbf{L}$)$_2$ 1433 cm^{-1}] is attributed to a combination of enolato-imine C=C and phenanthridinyl C=N stretches. In contrast, boron complexes of this ligand set[38] show distinct signals for the $\nu_{\mathrm{C\text{–}O,stretch}}$ of the enolato-imine unit, which suggests that π-bonds of the N^O fragment are more delocalized in the zinc complexes, extending over all five atoms of the chelating unit. Consistent with this description, Mayer bond order analysis[40] of the enolato-imine π-bonds O1–C$^{\mathrm{CH3}}$–CH–C$^{\mathrm{CH3}}$–N2 yields bond orders of 1.48, 1.33, 1.32, 1.49, respectively. Atomic dipole-corrected Hirshfeld charges[41] indicate greater concentration of charge at the oxygen donor atom (-0.34) compared with the nitrogen donor atom (-0.16).

UV-Vis Absorption and Emission Spectroscopy

All three complexes are yellow solids which dissolve in CH_2Cl_2 to produce intense yellow solutions. Their UV-Vis absorption spectra lack prominent features in the visible region and are reminiscent of the proligands which attenuate at ~400 nm (Figure S5).[37] A low energy tail stretching to ~475 nm accounts for the color of all three complexes. Three notable features are evident in the UV, with relatively well-resolved maxima evident at ~300, ~320 and ~365 nm that are invariant to ligand substitution (Figure 2, Table 1). Similar features have been observed in the proligands and in Pt(II) complexes with phenanthridinyl-based ligands related to those here.[33,37] A series of weak but well-resolved bands in this region is, in fact, typical of the ^1L_b π-π^* transitions of azaphenanthrenes including phenathridine.[42–44] In general, the lowest-energy singlet excited state of azaphenanthrene heterocycles like phenanthridine is comparable to that of the parent all-hydrocarbon phenanthrene, notwithstanding the inclusion of a heteroatom, and the energy is fairly insensitive to the local environment. Here, only slight solvatochromism was observed (Figure S6), consistent with this assignment.

All three complexes display weak, yellow luminescence in degassed dichloromethane solution at room temperature with quantum yields < 1%. The spectra are broad and largely unstructured. The emission maxima of $\mathrm{Zn}(^{t\mathrm{Bu}}\mathbf{L})_2$ and $\mathrm{Zn}(^{\mathrm{Me}}\mathbf{L})_2$ are very similar, while that of $\mathrm{Zn}(^{\mathrm{CF3}}\mathbf{L})_2$ is somewhat blue-shifted. The corresponding excitation spectra are shown in Figure S7. It was not possible to reliably determine emission lifetimes under these conditions, but we note that the emission intensity is significantly reduced upon aeration. A similar quenching response upon introduction of $^3O_2$ was observed for phosphorescent, 'caged' Zn tris-bipyridine complexes, but not for their uncaged, fluorescent congeners.[45] This implies that the excited state responsible for emission from $\mathrm{Zn}(^{\mathrm{R}}\mathbf{L})_2$ is itself relatively long-lived, or that it is being populated from a long-lived excited state. It is also notable that the emission (λ_{max} around 550 nm) is substantially red-shifted relative to the short-lived fluorescence displayed by the proligands under the same conditions, for which λ_{max} is < 500 nm in each case (Table S1).

At 77 K in an EPA glass, the spectra are all shifted to higher energy (λ_{max} ~ 500 nm; EPA = diethyl ether / isopentane / ethanol, 2:2:1 v/v; Figure S8). The emission is long-lived under these conditions, with average lifetimes > 100 ms, suggestive of phosphorescence from a triplet state. In comparison, pseudo-octahedral Zn(II) complexes of (*E*)-*N′*-((*E*)-(hydroxyimino)butan-2-ylidene)salicyloylhydrazide ligands have been reported to emit with λ_{max} = 550 nm as a *N,N*-dimethylformamide solvate and λ_{max} = 590 nm in their pure form.[23] Again, it is interesting to contrast the behaviour with that of the proligands. At 77 K, they display two distinct sets of vibrationally structured bands (Figure S5). The bands in the region 400 – 450 nm decay with a lifetime of around 1 ns, whereas the longer-wavelength bands ≥ 500 nm, have an emission lifetime of around 200 ms (Table S1). These properties are typical of fluorescence and phosphorescence, respectively, from *N*-heterocycles.

Solid-state samples of Zn($^{\mathbf{R}}\mathbf{L}$)$_2$ display quite bright yellow emission, with similar λ_{max} values around 540 nm at room temperature. The emission is visually brightest for Zn($^{\mathbf{Me}}\mathbf{L}$)$_2$ and weakest for Zn($^{\mathbf{CF3}}\mathbf{L}$)$_2$. Quantum yields recorded on powdered samples in an integrating sphere confirm this trend and range from 1- 6 % (Table 1). The average lifetimes are reduced compared to those in a frozen glass to around 25 ms (decay traces are shown in Figures S9-S10). Interestingly, the excitation spectra of the solid samples show an extra band at ~460 nm that is not present in dilute solution (Figure 2b). Indeed, the packing diagrams of the two crystallographically characterized complexes reveal intermolecular distances typical of luminogens exhibiting aggregation or crystallization-induced luminescence[46] [Zn($^{\boldsymbol{t}\mathbf{Bu}}\mathbf{L}$)$_2$ 3.5-3.7 A; Zn($^{\mathbf{CF3}}\mathbf{L}$)$_2$ 3.2-3.5 Å;

Figure S1]. A representative powder X-ray diffractogram of Zn($^{t\mathbf{Bu}}$**L**)$_2$ is provided as Figure S11. The proligands, in contrast, show only very weak emission in the solid state, at substantially higher energy. The weakness of the emission coupled with the high-energy excitation led to poor spectra; that for the brightest, $^{\mathbf{Me}}$**LH**, is given in Figure S12. Evidently, the zinc has a profound effect on the aggregation process and/or the subsequent emission. Aggregation-induced enhanced emission from aryl-decorated, non-planar Zn(II) β-diketiminate complexes has been reported.[47] In comparison to Zn($^{\mathbf{R}}$**L**)$_2$, such nacnac-supported, tetrahedral Zn complexes emit in fluid solution with smaller Stokes' shifts (300 cm^{-1}) and ~12 ns lifetimes consistent with fluorescence.[48]

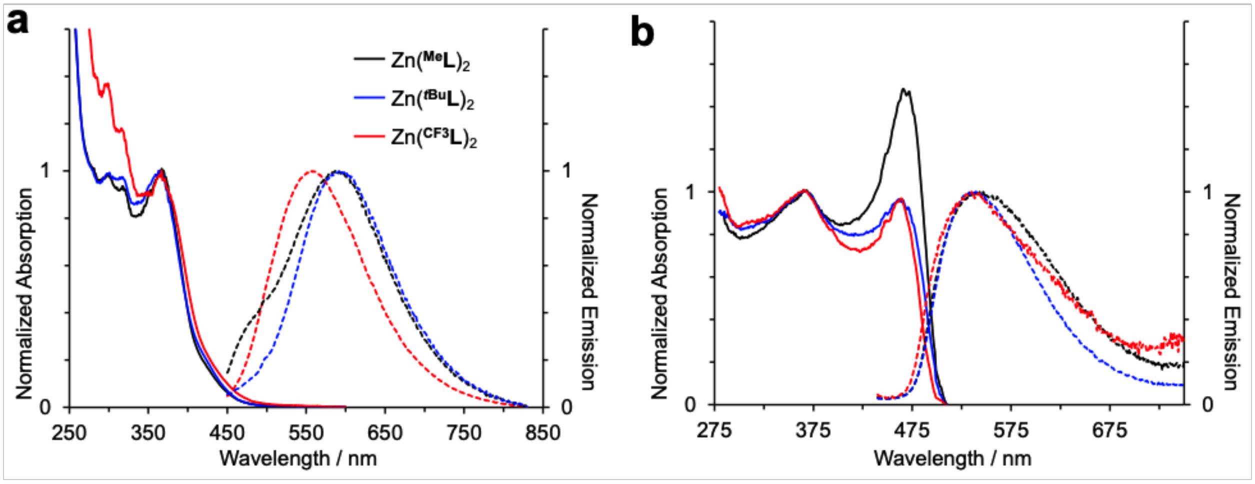

Figure 2. Normalized (a) UV-vis absorption and emission spectra of Zn($^{\mathbf{R}}$**L**)$_2$ in CH_2Cl_2 at 295 K (λ_{ex} = 432 nm) and (b) emission spectra (λ_{ex} = 400 nm) and excitation spectra (λ_{em} = 540 nm) in the solid state at 295 K (Note: identical emission spectra were observed using λ_{ex} = 460 nm).

Table 1. Photophysical and electrochemical data for Zn(${}^{\mathbf{R}}\mathbf{L}$)$_2$

Complex	**Absorption**^{a} **λ_{max} / nm (ε / M^{-1} cm^{-1})**	**Emission at 295 K**^{a} **λ_{max} / nm**	**Emission 77 K**^{b}		**Emission Solid-State 295 K**			***E*$_{1/2}$ / V**^{d,e}
			λ_{max} / nm	**τ / ms**	**λ_{max} / nm**	**τ / ms**	**Φ**^{c}	
Zn(${}^{\mathbf{Me}}\mathbf{L}$)$_2$	298 (14 430), 317 (14 550), 364 (15 830)	587	510	190	543	25	4.4	0.22, 0.58
Zn(${}^{t\mathbf{Bu}}\mathbf{L}$)$_2$	298 (19 190), 317 (20 020), 366 (21 330)	593	503	120	539	27	6.0	0.22, 0.59
Zn(${}^{\mathbf{CF3}}\mathbf{L}$)$_2$	288 (14 150), 328 (13 040), 367 (15 450)	557	500	160	536	22	1.0	-2.21^{f}, 0.39, 0.69

[a] in CH_2Cl_2

[b] in EPA glass [EPA = diethyl ether / isopentane / ethanol (2:2:1 v/v)][49]

[c] Measured using an integrating sphere, with a sample of finely powdered $BaSO_4$ as a non-emissive blank.

[d] vs FcH$^{0/+}$ in CH_2Cl_2 at scan rates of 100 mV s^{-1}.

[e] Irreversible.

[f] Reduction

Electronic Structures

DFT and TDDFT calculations were carried out to investigate the electronic structures of Zn($^{\mathbf{R}}$**L**)$_2$. Gas-phase optimized geometries of the Zn(II) complexes [ZORA-B3LYP-D3(BJ)/def2-SV(P)] accurately reproduce the solid-state structures (Table S2). Single-point calculations with implicit solvation (SMD, CH_2Cl_2) were performed on the ground-state equilibrium geometries to model the frontier molecular orbitals (Figure 3; see Tables S3-S5 for fragment contributions). The two highest filled MOs of Zn($^{\mathbf{R}}$**L**)$_2$ are largely comprised of the enolato-imine N^O moiety (~60%) and are nearly degenerate. The energy difference between the two highest filled MOs found by DFT ($\Delta E_{\text{HOMO-HOMO-1}}$ = 0.14 eV) is in broad agreement with that estimated by cyclic voltammetry ($\Delta E_{\text{HOMO-HOMO-1}}$ = 0.30-0.37 eV; Figure 4, Table 1). The two lowest-lying, nearly degenerate vacant MOs ($\Delta E_{\text{LUMO-LUMO+1}}$ < 80 meV) are largely phenanthridinyl-based (~90%) with significant density at the N=C*H* sub-unit (~30%). An electrochemical reduction can be clearly observed only for Zn($^{\mathbf{CF3}}$**L**)$_2$ (-2.21 V; -2.36 eV); cathodic events for Zn($^{\mathbf{Me/\mathit{t}Bu}}$**L**)$_2$ overlap with the solvent window. This shift to less negative potential for Zn($^{\mathbf{CF3}}$**L**)$_2$ is again in line with calculated LUMO values. Pseudo-square planar Pt(II) complexes of $^{\mathbf{R}}$**L** with a chloride co-ligand exhibit similar localization of the HOMO electron density at the N^O core, but with significant mixing between filled Pt(II) *d*-orbitals and chloride lone-pair of the appropriate π-type symmetry.[37] In such Pt(II) complexes, the LUMO orbital density is similarly localized on the phenanthridinyl moiety. Interestingly, the HOMO and HOMO-1 in Zn($^{\mathbf{R}}$**L**)$_2$ show weak, but not completely negligible, pπ-dπ mixing (< 2%) of the N2 and O1 lone pairs with Zn(II) *d*-orbitals of appropriate symmetries. In combination with the diminished amido character of the ligand upon coordination to Zn(II), this pπ-dπ mixing could contribute to the enhanced stability of the present complexes to air and ambient moisture compared to homoleptic *N*-phenyl-phenanthridinylamidozinc(II) complexes.[39]

Participation of metal *d*-orbitals in electronic transitions should also promote both intersystem crossing (ISC) to low-lying excited triplet states and the subsequent radiative decay of the T_1 state to generate phosphorescence (*vide infra*).

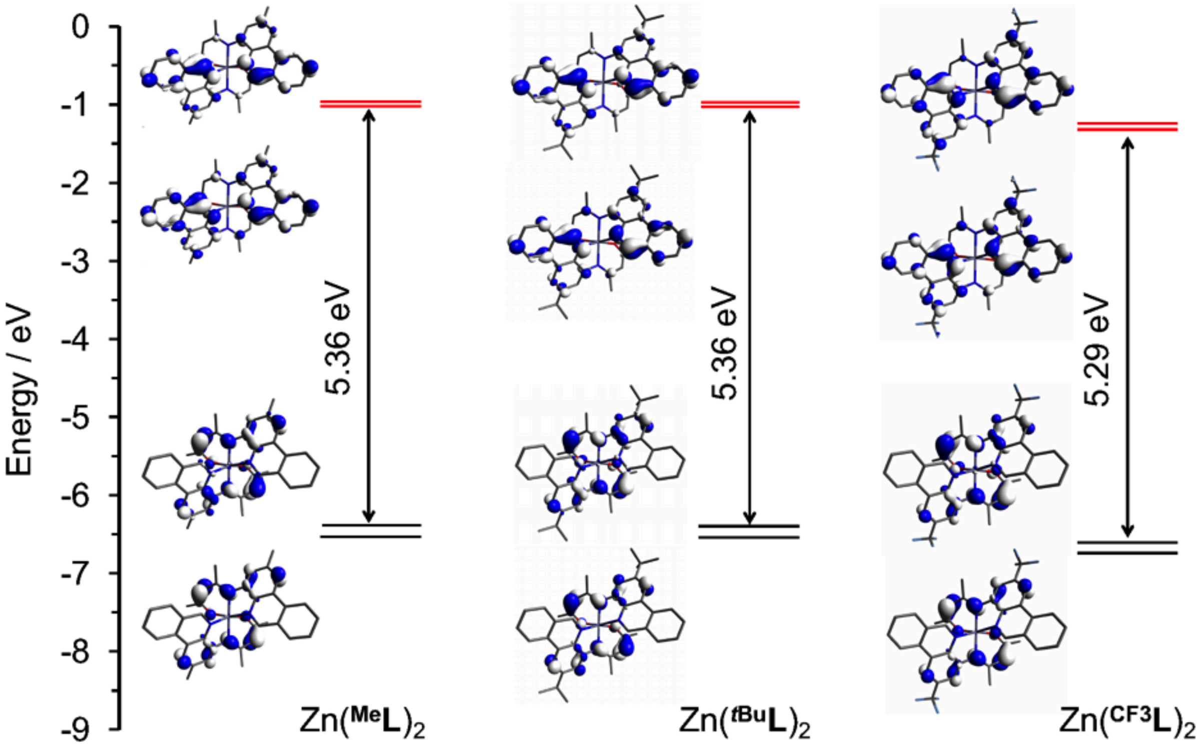

Figure 3. Ground-state frontier molecular orbital energy level diagram (HOMO-1 to LUMO+1), HOMO-LUMO energy gaps and isosurfaces (isovalue = 0.04) for Zn(^{R}**L**)$_2$.

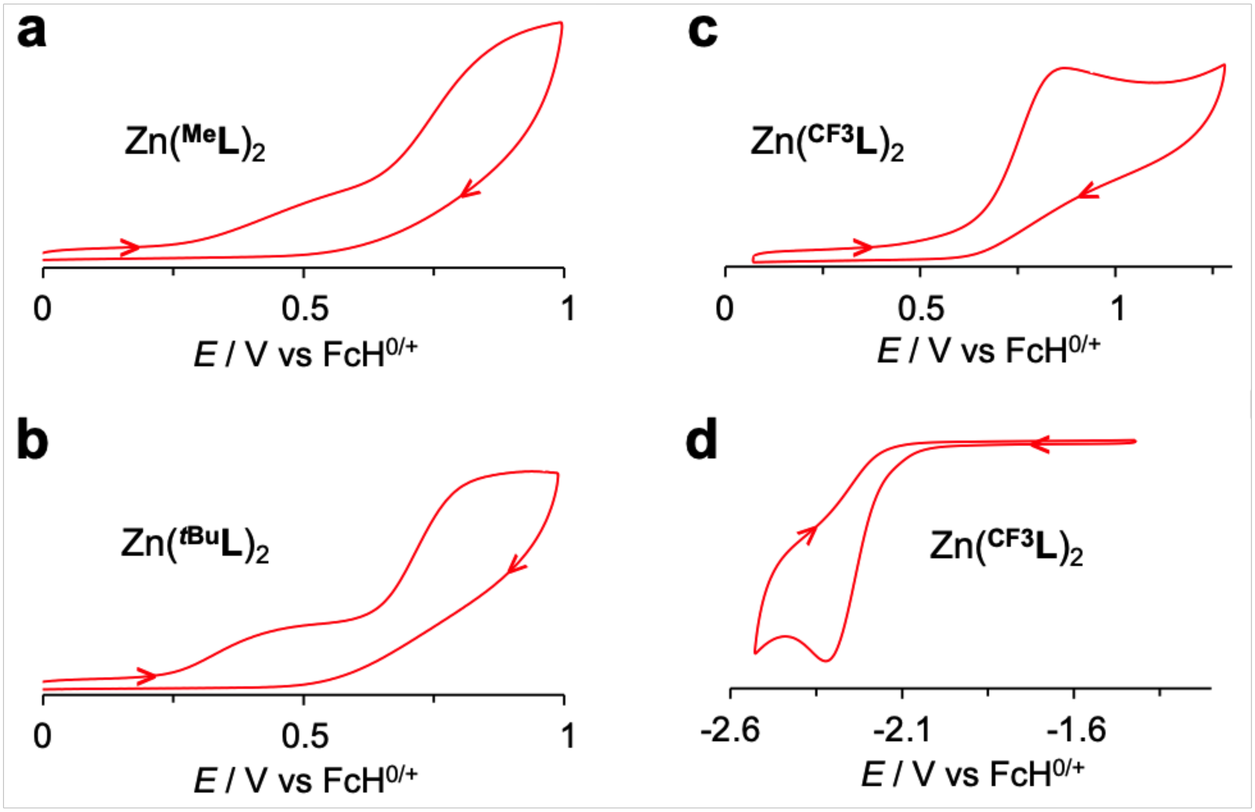

Figure 4. Cyclic voltammograms of (a) Zn($^{\mathbf{Me}}$**L**)$_2$, (b) Zn($^{t\mathbf{Bu}}$**L**)$_2$, (c) and (d) Zn($^{\mathbf{CF_3}}$**L**)$_2$ performed in a 1 mM CH_2Cl_2 solution containing 100 mM [*n*Bu$_4$N][PF$_6$] as supporting electrolyte and 100 mv/s scan rate.

Overall, the orbital characters of the frontier MOs imply that intraligand charge-transfer (ILCT) dominates the lowest energy absorption manifold ($\lambda_{abs} > 375$ nm) and contributes to the low energy tail observed in all complexes. To support this assignment, scalar-only relativistic TDDFT calculations on the gas-phase optimized ground-state geometries of the complexes were conducted in CH_2Cl_2 (Figures S13-S15, Tables S6-S8). These predict two electronic transitions with oscillator strengths > 0.1. The lowest energy vertical excitations (S_1) are dominantly HOMO→LUMO in character (> 60%), with minor contribution from the HOMO-1→LUMO+1 (> 10%). The second lowest-lying excited singlet state largely consists of HOMO→LUMO+1 (~50%) and HOMO-1→LUMO excitations. Scalar-only TDDFT, therefore, supports ILCT character of the lowest energy absorption manifold of the complexes, with the low-energy tail associated with the HOMO→LUMO excitation accounting for the intense yellow color of the complexes. This implies that exciton pairs generated from the two lowest-lying excited singlet states are highly delocalized between the two ligands.

Electron-hole density maps are consistent with ILCT with electron transfer from the N^O chelate rings to the phenanthridinyl-acceptor moieties. While a CT assignment might imply a strong influence of the solvent dielectric, the complexes exhibit weak solvatochromism of the $\lambda_{max,abs}$ (Figure S6); more prominent shifts are observed for the low-energy shoulder. Fe(II) complexes supported by 4-[*N*-(8-quinolinyl)]amidophenanthridines, also with approximate C_2 symmetry, exhibit CT excitations (pπ/dπ*-to-ligand CT or 'π-anti-bonding-to-ligand' PALCT) occurring between 600-800 nm and are similarly invariant to changes in solvent polarity,[35,50] as is the MLCT band of $[Ru(bpy)_3]^{2+}$, which shows only weak solvatochromism.[51] In each case, the complexes exhibit a more spherically symmetric redistribution of the electron density. As mentioned above, electron-hole density maps reveal a rather symmetric and delocalized redistribution of the exciton pair between ligands which may account for the weak solvatochromism.

The characteristics and trends in the emission of the complexes warrants further discussion. The millisecond (ms) lifetimes and the size of the apparent Stokes shift (1.2-1.3 eV) suggest that radiative decay occurs from a long-lived excited triplet state. To understand the decay process from the initially populated ^{1}ILCT states, the minima of the lowest energy excited singlet and triplet states were optimized. Figures S16-S18 show the relevant photophysical parameters for the complexes in CH_2Cl_2 that can then be extracted. TDDFT assigns the lowest-lying excited singlet state as a ligand-to-ligand charge-transfer state (^{1}LLCT) based on its electron-hole density map, with the electron localized in the phenanthridinyl moiety of one of the ligands and the hole predominantly in the *N^O* fragment of the other. In contrast, the spin density of the lowest-lying excited triplet state has both the electron and the hole localized in the same ligand unit and is thus assigned as a symmetry-broken intraligand charge-transfer triplet (^{3}SBCT). These results suggest that the symmetry of the initially populated ^{1}ILCT is broken upon relaxation. This assignment is invariant to the degree of Hartree-Fock admixture introduced (Figure S19). Such symmetry-broken charge transfer (SBCT) states have been observed in bis(dipyrrin)zinc(II) and are thought to promote efficient ISC to low-lying triplet manifolds either through radical pair ISC (RP-ISC) or spin-orbit charge transfer ISC (SOCT-ISC).[52–55] To our knowledge, however, bis(dipyrrin)zinc(II) do not exhibit detectable phosphorescence either in solution or the solid state, unlike Zn($^{\mathbf{R}}$**L**)$_2$. The driving force for charge-separation, ΔG_{CS},[56,57] in Zn($^{\mathbf{CF_3}}$**L**)$_2$ was estimated (neglecting Coulombic interactions between the electron-hole pair, E_c) to be -0.78 eV in CH_2Cl_2, using Equation (1) where e is the elementary charge, $E_{\mathrm{ox/red}}$ are the oxidation and reduction potentials observed for Zn($^{\mathbf{CF_3}}$**L**)$_2$ and E* (the energy of the excited state) is estimated from $\lambda_{\max}$(absorption)[58]:

$$\Delta G_{\mathrm{CS}} = e[E_{\mathrm{ox}}(D) - E_{\mathrm{red}}(A)] - E^* - E_\mathrm{c} \qquad (1)$$

Across the Zn($^{\mathbf{R}}$**L**)$_2$ series, fluorescence energies ($\Delta E^{\mathrm{fluor}}$) calculated in a polarizable continuum (CH_2Cl_2) at room temperature are considerably higher than the experimentally observed emission [Zn($^{\mathbf{Me}}$**L**)$_2$: 3.00 eV *cf.* 2.11 eV (experimental); Zn($^{\mathbf{CF_3}}$**L**)$_2$: 2.92 eV *cf.* 2.23 eV (experimental); see Figures S16-S18]; a much better match is obtained comparing the experimentally observed emission energies with those calculated for a phosphorescence-type process [ΔE^{phos}; Zn($^{\mathbf{Me}}$**L**)$_2$: 2.09 eV *cf.* 2.11 eV (experimental); Zn($^{\boldsymbol{t}\mathbf{Bu}}$**L**)$_2$: 1.81 eV *cf.* 2.09 eV (experimental); Zn($^{\mathbf{CF_3}}$**L**)$_2$: 2.06 eV *cf.* 2.23 eV (experimental)]. This supports phosphorescence as the predominant radiative decay pathway for the complexes, originating from low-lying ^{3}SBCT states.

Spin-orbit coupling (SOC) matrix elements (SOCMEs) were also calculated (Tables S9-S11). These indicate weak but non-vanishing mixing between excited singlet and triplet states, which is commensurate with the efficiency of intersystem-crossing (ISC) from an initially populated ^{1}ILCT to the excited triplet state manifold and may explain the ms lifetimes observed for all complexes. The eight lowest triplet excited states at the ground-state geometry all exhibit coupling with the two lowest-lying excited singlet states such that ISC might occur (i) from ^{1}ILCT$_1$ or ^{1}ILCT$_2$ to any of these lower-lying excited triplet states before decaying to the emissive triplet state; or (ii) via direct ISC to the emissive triplet state. Furthermore, these triplet excited states are also weakly coupled to the ground state, which may contribute to the low quantum yield.

The observed Stokes shift can be accounted for by the combined energy losses from ISC (λ^{ISC}) and ground state reorganization (λ^{T}) with calculated values between 1.1-1.3 eV. Structural comparisons between the optimized ground-state geometry ($S_{0,eq}$) and the lowest-lying triplet state (^{3}SBCT$_{eq}$) reveal an asymmetric elongation of the ligands (Figure 5, Table S12). Further elongation Zn-N/O bonds for this same ligand unit is observed in the optimized geometry of the lowest-lying excited singlet excited state (^{1}LLCT$_{eq}$), which could contribute to the nonradiative dissipation of energy of the complexes in solution. In addition, the O1-Zn-O2 bond angle decreases upon relaxation to the T_1 minima by 9°, while the N1-Zn-N1'/N1-Zn-N3 bond angle opens by 8°. Such molecular distortions should be attenuated in frozen glass at 77 K and in the solid state, consistent with the observed blue-shift in emission and increased emission intensity compared with in fluid solution. The energy of the lowest-lying triplet state at the ground state geometry, calculated using the energy difference between the energies of ^{3}SBCTand $S_{0,eq}$, mirrors this hypsochromic effect [Zn($^{\mathrm{Me}}$**L**)$_2$: 2.92 eV *cf.* 2.43 eV (77 K), 2.28 eV (solid); Zn($^{t\mathrm{Bu}}$**L**)$_2$: 2.49 eV *cf.* 2.46 eV (77 K), 2.30 eV (solid); Zn($^{\mathrm{CF3}}$**L**)$_2$: 2.84 eV *cf.* 2.48 eV (77 K), 2.31 eV (solid); see Figures

S16-S18]. Close inspection of the solid-state structures of Zn(^{tBu}**L**)$_2$ and Zn(^{CF3}**L**)$_2$ suggest that molecules are rigidified in the solid state through noncovalent π-stacking (staggered and T-shaped) interactions (Figure S1). Aggregation-enhanced emission has been reported for fluorescent homoleptic, four-coordinate Zn(II) complexes ligated by arene-rich β-diketiminates where noncovalent interactions in the solid state restrict the rotations of the aryl substituents.[47] In contrast, *bis*[phenanthridinyl-4-(*N*-phenyl)amidozinc(II)] complexes do not exhibit any appreciable luminescence upon excitation of the ^{1}ILCT band (~500 nm) and excitation at higher energies shows emission that strongly overlaps with the ILCT absorption manifold.[39] The results presented here suggest that emission can be 'turned on' in Zn(II) complexes supported by N^N^O amido-type frameworks, through increased delocalization of the nitrogen lone pair and enhanced rigidity through saturating the coordination environment of the metal.

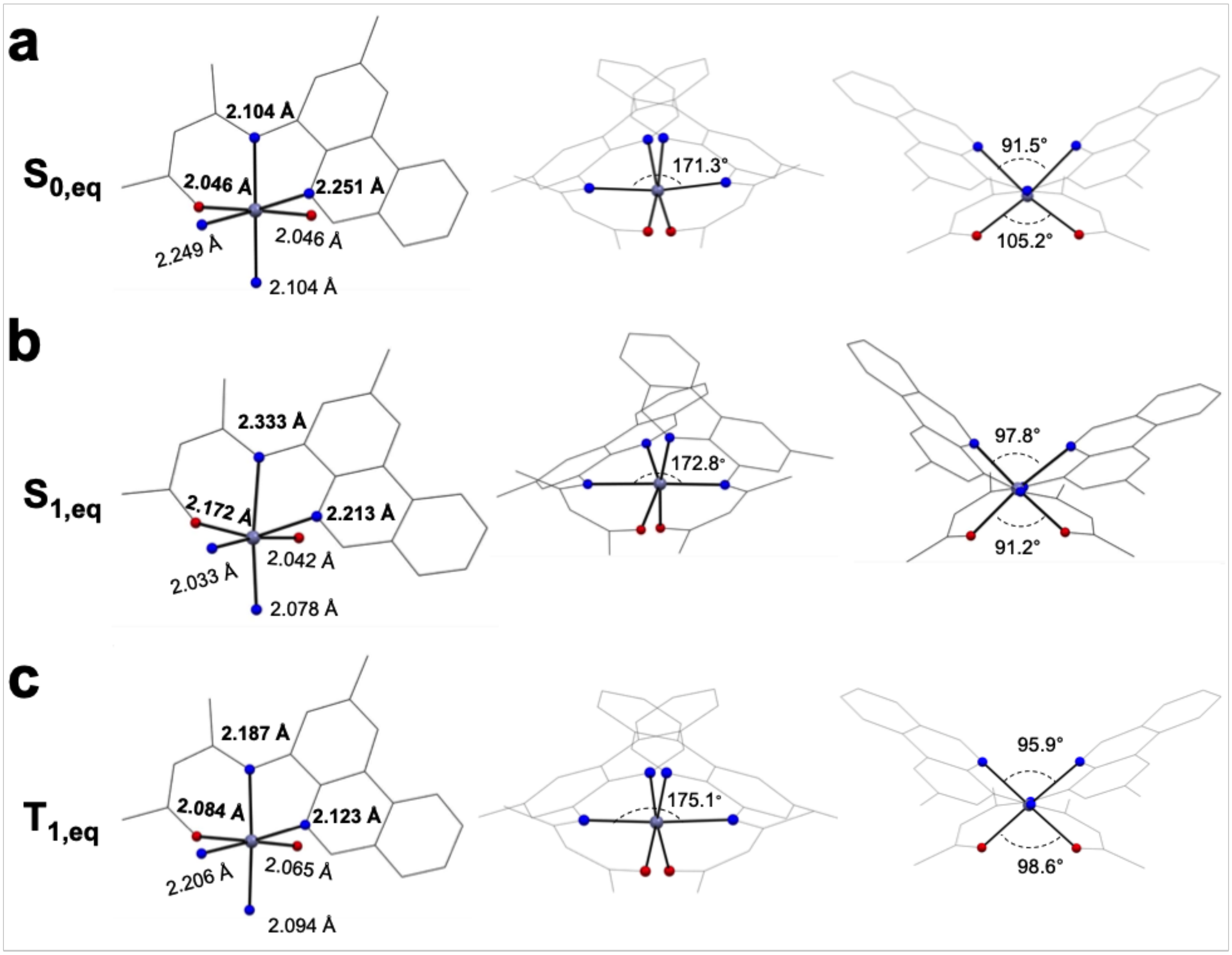

Figure 5. Select structural parameters for the gas-phase optimized geometries of (a) ground state ($S_{0,eq}$), (b) the lowest-lying excited singlet ($S_{1,eq}$), and (c) the lowest-lying excited triplet state ($T_{1,eq}$) for Zn($^{\mathbf{Me}}\mathbf{L}$)$_2$.

Conclusions

Three Zn(II) complexes, Zn($^{\mathbf{R}}\mathbf{L}$)$_2$, supported by monoanionic, tridentate N^N$^-$^O ligands containing phenanthridinyl donors are presented. These exhibit yellow emission in solution and in the solid state, with millisecond lifetimes consistent with radiative relaxation from a low-lying emissive excited triplet state. This is in contrast to the non-emissive character of related phenanthridinyl amide-supported tetradentate Zn(II) complexes with pronounced N_{amido} character to the ligand. These findings suggest that attenuating the N_{amido} character, through the combination of non-negligible pπ-dπ mixing in a stronger (pseudo)octahedral ligand field and delocalization through the acetyl-acetone derived ligand arm, may provide a mechanism for 'turning on' emission from long-lived triplet states in *N*-heterocycle/amido supported Zn(II) coordination compounds.

Experimental Section

General Considerations

Air-sensitive manipulations were carried out in a N_2-filled glove box or using standard Schlenk techniques under Ar. Organic solvents were dried and distilled using appropriate drying agents. Diethylzinc (1 M in hexanes) was purchased from Sigma-Aldrich. **^{R}LH** were synthesized according to previously published procedures.[36,38] 1- and 2D NMR spectra were recorded on a Bruker Avance 300 MHz spectrometer or a Bruker Avance 500 MHz spectrometer. ^{1}H and $^{13}C\{^{1}H\}$ NMR spectra were referenced to residual solvent peaks. High resolution mass spectra were recorded using a Bruker microTOF-QIII. Attenuated total reflectance infrared spectroscopy (ATR-IR) was performed using a Bruker Invenio R FTIR. For electrochemical analysis, 5-10 mg of each compound was dissolved in 15 mL of 0.1 M $[n\mathrm{Bu}_4\mathrm{N}][\mathrm{PF}_6]$ in CH_2Cl_2. The measurements were performed on the solutions in an N_2-filled glovebox using a CHI 760c bipotentiostat, a 3 mm diameter glassy carbon working electrode, a $Ag^{+} | Ag$ quasi-non-aqueous reference electrode separated by a Vycor tip, and a Pt wire counter electrode. Cyclic voltammetry was conducted using a scan rate of 100 mV/s. Upon completion, ferrocene (FcH) was added to the solution as an internal standard, and all potentials are reported versus the $FcH^{+} | FcH$ redox couple.

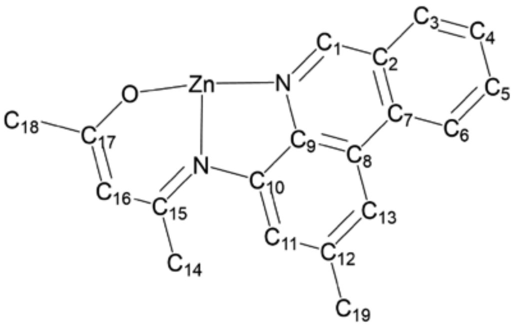

Synthesis of Zn(^{Me}L)$_2$. To a cooled solution of $^{\mathbf{Me}}$**LH** (0.105 g, 0.360 mmol) in hexanes/toluene (7.5 mL/2.5 mL, -38 °C), a cooled solution of diethylzinc (1 M in hexanes; 250 μL, 0.25 mmol; -38 °C) was added dropwise and the mixture left stirring overnight at room temperature, over which period the solution color changed from a pale to intense yellow with formation of a yellow precipitate. The solvent was removed *in vacuo* and the resulting residue was repeatedly washed with cyclohexane, then crystallized by cooling solutions of the product prepared in hot cyclohexane. Yield = 0.0836 g (84%). ^{1}H NMR (CDCl$_3$, 300 MHz, 25 °C): δ 8.58 (s, 1H, C$_1$*H*), 8.40 (d, $^3J_{HH}$ = 8.7 Hz; 1H, C$_6$*H*), 7.65-7.80 (m, 3 H, C$_{3,5,13}$*H*), 7.54 (ddd, $^3J_{HH}$ = 7.5, 8.8 Hz, $^4J_{HH}$ = 0.8 Hz; 1H, C$_4$*H*), 7.16 (d, $^4J_{HH}$ = 1.1 Hz; 1H, C$_{11}$*H*), 5.08 (s, 1H, C$_{16}$*H*), 2.52 (s, 3H, C$_{19}$*H*), 2.27 (s, 3H, C$_{14}$*H*), 1.79 (s, 3H, C$_{18}$*H*). ^{13}C{^{1}H} NMR (CDCl$_3$, 75 MHz, 25 °C): δ 187.5 (C$_{17}$), 168.4 (C$_{15}$), 157.0 (C$_1$), 144.1 (C$_{10}$), 135.4 (C$_{12}$), 134.6 (C$_9$), 132.4 (C$_5$), 130.4 (C$_3$), 126.7 (C$_4$ and C$_8$), 126.0 (C$_7$), 123.4 (C$_2$), 123.1 (C$_{11}$), 122.4 (C$_6$), 114.6 (C$_{13}$), 99.4 (C$_{16}$), 28.1 (C$_{19}$), 23.0 (C$_{18}$), 22.3 (C$_{14}$). HRMS (ESI-TOF) m/z: [M + H]$^+$ Calcd for [$C_{38}H_{35}N_4O_2Zn$]$^+$ 643.2046; Found 643.2066.

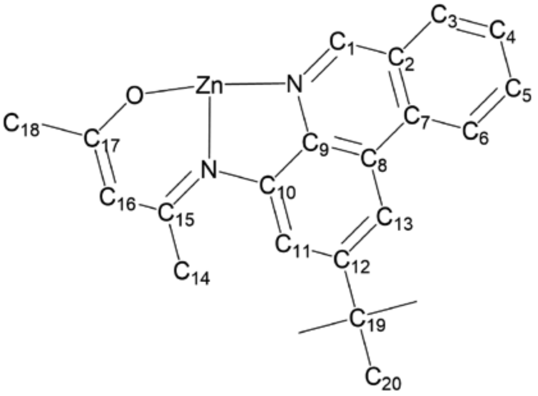

Synthesis of Zn(^{tBu}L)$_2$. The procedure was the same as for Zn($^{\mathbf{Me}}$**L**)$_2$ starting from $^{t\mathbf{Bu}}$**LH** (0.104 g, 0.312 mmol) in hexanes/toluene (7.5 mL/2.5 mL, -38 °C), and diethylzinc (1 M in hexanes; 220 μL, 0.22 mmol; -38 °C). Yield = 0.0607 g (54%), yellow solid. ^{1}H NMR (CDCl$_3$, 300 MHz, 25 °C): δ 8.57 (s, 1H, C$_1$*H*), 8.43 (d, $^3J_{HH}$ = 8.4 Hz; 1H, C$_6$*H*), 7.90 (d, $^4J_{HH}$ = 1.4 Hz; 1H, C$_{13}$*H*), 7.65-7.78 (m, 2H, C$_3$*H* and C$_5$*H*), 7.52 (ddd, $^3J_{HH}$ = 7.3, 8.5 Hz, $^4J_{HH}$ = 1.0 Hz; 1H, C$_4$*H*), 7.46 (d, $^4J_{HH}$ = 1.5 Hz; 1H, C$_{11}$*H*), 5.13 (s, 1H, C$_{16}$*H*), 2.30 (s, 3H, C$_{14}$*H*), 1.82 (s, 3H, C$_{18}$*H*), 1.44 (s, 9H, C$_{20}$*H*). ^{13}C{^{1}H} NMR (CDCl$_3$, 75 MHz, 25 °C): δ 187.7 (C$_{17}$), 168.4 (C$_{15}$), 149.8 (C$_{12}$), 149.2 (C$_1$), 145.0 (C$_{10}$), 134.7 (C$_9$), 133.2 (C$_5$), 131.1 (C$_8$), 129.2 (C$_3$), 127.0 (C$_4$), 126.2 (C$_2$), 123.7 (C$_7$), 122.2 (C$_6$), 120.3 (C$_{11}$), 110.5 (C$_{13}$), 100.1 (C$_{16}$), 35.4 (C$_{19}$), 31.5 (C$_{20}$), 28.4 (C$_{18}$), 23.0 (C$_{14}$). HRMS (ESI-TOF) m/z: [M + H]$^+$ Calcd for [$C_{44}H_{47}N_4O_2Zn$]$^+$ 727.2985; Found 727.3040.

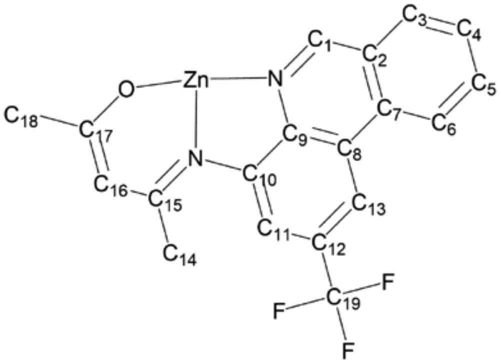

Synthesis of Zn($^{\mathbf{CF3}}$L)$_2$. The procedure was the same as for Zn($^{\mathbf{Me}}$**L**)$_2$, starting from $^{\mathbf{CF3}}$**LH** (0.117 g, 0.340 mmol) in hexanes/toluene (7.5 mL/2.5 mL, -38 °C), and diethylzinc (1 M in hexanes; 240 μL, 0.24 mmol; -38 °C). Yield = 0.100 g (79%), yellow solid. ^{1}H NMR (CDCl$_3$, 300 MHz, 25 °C): δ 8.70 (s, 1H, C$_1$*H*), 8.41 (d, $^3J_{HH}$ = 8.2 Hz; 1H, C$_6$*H*), 8.13 (s, 1H, C$_{13}$*H*), 7.77-7.90 (m, 2H, C$_3$*H* and C$_5$*H*), 7.66 (ddd, $^3J_{HH}$ = 7.4, 8.5 Hz, $^4J_{HH}$ = 0.8 Hz; 1H, C$_4$*H*), 7.50 (d, $^4J_{HH}$ = 1.5 Hz; 1H, C$_{11}$*H*), 5.20 (s, 1H, C$_{16}$*H*), 2.30 (s, 3H, C$_{14}$*H*), 1.84 (s, 3H, C$_{18}$*H*). ^{19}F NMR (CDCl$_3$, 282 MHz, 25 °C): δ 62.35 (s, C$_{19}$*F*). ^{13}C{^{1}H} NMR (CDCl$_3$, 75 MHz, 25 °C): δ 189.7 (C$_{17}$), 168.8 (C$_{15}$), 151.9 (C$_1$), 146.5 (C$_{10}$), 137.4 (C$_9$), 132.8 (C$_7$), 132.4 (C$_5$), 129.5 (C$_3$), 128.8 (q, $^2J_{CF}$ = 32.1 Hz; C$_{12}$), 128.4 (C$_4$), 126.1 (C$_8$), 124.2 (C$_2$), 122.3 (C$_6$), 117.0 (q, $^3J_{CF}$ = 3.3 Hz; C$_{11}$), 111.7 (q, $^3J_{CF}$ = 4.4 Hz; C$_{13}$), 101.0 (C$_{16}$), 28.6 (C$_{18}$), 22.9 (C$_{14}$). HRMS (ESI-TOF) m/z: [M + H]$^+$ Calcd for [$C_{38}H_{29}N_4O_2Zn$]$^+$ 751.1481; Found 751.1552.

X-Ray Crystallography Experimental Details

X-ray crystal structure data were collected from multi-faceted crystals of suitable size and quality, selected from a representative sample of crystals of the same habit using an optical microscope. Crystals were mounted on MiTiGen loops and data collection was carried out in a cold stream of nitrogen (150 K; Bruker D8 QUEST ECO). Diffractometer manipulations were carried out using Bruker APEX3 software.[59] Structure solution and refinement were performed using XS, XT and XL software, embedded within the OLEX2.[60] For each structure, the absence of additional symmetry was confirmed using ADDSYM incorporated in the PLATON program.[61] PXRD patterns were acquired in a Bruker D8 Advance diffractometer (Cu Kα) using a room temperature rotation stage.

Crystal structure data of Zn($^{t\mathrm{Bu}}$L)$_2$ (CCDC 2119917): X-ray quality crystals were grown following layering of hexanes into a CH_2Cl_2 solution at room temperature. Crystal structure parameters: $C_{45}H_{48}Cl_2N_4O_2Zn$ 813.14 g/mol, monoclinic, space group $P2_1/n$; $a = 20.825(3)$ Å, $b = 8.8858(11)$ Å, $c = 22.615(3)$ Å, $\alpha = \gamma = 90°$, $\beta = 102.594(5)°$, V = 4084.2(9) Å^3; Z = 4, $\rho_{\mathrm{calcd}} = 1.322$ g cm^{-3}; crystal dimensions 0.32 x 0.13 x 0.05 mm; diffractometer Bruker D8 QUEST ECO CMOS; Mo K_α radiation, 150(2) K, $2\theta_{\max} = 2.502$ to 24.415°; 34008 reflections, 7174 independent ($R_{\mathrm{int}} = 0.0648$), direct methods; absorption coeff ($\mu = 0.686$ mm^{-1}), absorption correction semi-empirical from equivalents (SADABS); refinement (against F_o^2) with SHELXTL V6.1, 497 parameters, 0 restraints, $R_1 = 0.1147$ ($I > 2\sigma$) and $wR_2 = 0.2041$ (all data), Goof = 1.123, residual electron density 1.190/−1.587 e Å^{-3}.

Crystal structure data of Zn(^{CF3}L)$_2$ (CCDC 2119918): X-ray quality crystals were grown following layering of hexanes into a benzene solution. Crystal structure parameters: $C_{44}H_{42}F_6N_4O_2Zn$ 838.18 g/mol, monoclinic, space group $C2/c$; $a = 10.4717(6)$ Å, $b = 12.3015(6)$ Å, $c = 30.9829(16)$ Å, $\alpha = \gamma = 90°$, $\beta = 90.077(2)°$, V = 3991.1(4) Å^3; Z = 4, $\rho_{calcd} = 1.395$ g cm^{-3}; crystal dimensions 0.45 x 0.26 x 0.09 mm; diffractometer Bruker D8 QUEST ECO CMOS; Mo K_α radiation, 150(2) K, $2\theta_{max}$ = 2.554 to 30.628°; 64265 reflections, 6157 independent (R_{int} = 0.0468), direct methods; absorption coeff ($\mu = 6.804$ mm^{-1}), absorption correction semi-empirical from equivalents (SADABS); refinement (against F_o^2) with SHELXTL V6.1, 262 parameters, 0 restraints, $R_1 = 0.0684$ ($I > 2\sigma$) and $wR_2 = 0.1897$ (all data), Goof = 1.115, residual electron density 2.577/-1.313 e Å^{-3}.

UV-visible Absorption and Luminescence Measurements

Absorption spectra were measured on a Biotek Instruments XS spectrometer, using quartz cuvettes of 1 cm pathlength. Steady-state luminescence spectra in deoxygenated solution and in an EPA glass at 77 K were measured using a Jobin Yvon FluoroMax-2 spectrofluorimeter, fitted with a red-sensitive Hamamatsu R928 photomultiplier tube; the spectra shown are corrected for the wavelength dependence of the detector, and the quoted emission maxima refer to the values after correction. Samples for emission measurements were contained within quartz cuvettes of 1 cm pathlength modified with appropriate glassware to allow connection to a high-vacuum line. Degassing was achieved via a minimum of three freeze-pump-thaw cycles whilst connected to the vacuum manifold; final vapor pressure at 77 K was $< 5 \times 10^{-2}$ mbar, as monitored using a Pirani gauge. The spectra in the solid state were recorded by means of an integrating sphere attached to a Jobin Yvon Fluorolog instrument through optical fibers. Finely powdered samples were contained within Spectralon sample holders of 10 mm diameter. Quantum yields were determined using a sample of finely powdered $BaSO_4$ as a non-emissive blank.

Luminescence lifetimes were measured following excitation with a microsecond-pulsed xenon lamp and detection using a Hamamatsu R928 photomultiplier tube operating in multichannel scaling mode. For all measurements, the decays were much longer than the instrument response, and data were analyzed by tail fitting to the following equation (2):

$$I(\mathrm{t}) = I(0)\,\exp(-k\mathrm{t}) + \mathrm{c} \qquad (2)$$

where $I(\mathrm{t})$ is the intensity of light detected at time t, k is the first-order rate constant for decay ($k = 1/\tau$), and c is a constant reflecting the intrinsic "dark count" during the measurement. The data in solid-state fit well to the above equation, with no significant improvement upon introducing additional components. At 77 K, the data show evidence of an additional short-lived component and the values quoted in Table 1 refer to tail-fitting of the long component only.

Computational details

All computations were performed using ORCA v.4.2.1.[62,63] The zeroth order approximation (ZORA) were used in all calculations to account for scalar relativistic effects. No symmetry constraints were imposed on all calculations. Both restricted and unrestricted Kohn-Sham Density Functional Theory (KS-DFT) were employed for closed-shell and open-shell systems, respectively. Optimizations are performed in the gas phase with the B3LYP[64–66] functional augmented with Grimme's D3 dispersion correction and Becke-Johnson damping[67] (B3LYP-D3(BJ)) in combination with the recontracted Ahlrichs split-valence double-ζ basis set with polarization only on non-hydrogen atoms ZORA-def2-SV(P)[68]. B3LYP has been shown to accurately reproduce ground state geometries of Zn(II) coordination complexes.[69,70,23] Crystal structure coordinates for Zn($^{t\mathbf{Bu}}$**L**)$_2$ and Zn($^{\mathbf{CF3}}$**L**)$_2$ were used as starting input for ground state optimization ($S_{0,eq}$), while modified coordinates from Zn($^{t\mathbf{Bu}}$**L**)$_2$ were used for Zn($^{\mathbf{Me}}$**L**)$_2$, using Avogadro.[71] Coordinates from the ground-state equilibrium geometries were then used to optimize the lowest-lying excited singlet ($S_{1,eq}$) and triplet-state ($T_{1,eq}$) geometries. The $S_{1,eq}$ geometry for Zn($^{t\mathbf{Bu}}$**L**)$_2$ could not be optimized despite repeated attempts. DFT integration grids, optimization and SCF convergence criteria were set to grid5/finalgrid7, tightopt, and tightscf, respectively. Additional radial integration grid (specialgridatom, 30; specialgridintacc, 7, 7, 7) were implemented for Zn. "No resolution-of-identity" (nori) was employed for all optimizations. The absence of imaginary frequencies confirm that all optimized geometries are real minima. The transmission IR spectra of the complexes were simulated using Avogadro employing Lorentzian broadening (peak width: 20 cm^{-1}) and scaling factor of 0.9. Single-point calculations including TDDFT were performed using the M06 and M06-2X[72] functionals in combination with the recontracted Ahlrichs split-valence triple-ζ basis set with polarization on all atoms, ZORA-def2-TZVP[68], and including solvation effects using SMD[73] (CH_2Cl_2). We employed the RIJCOSX approximation as implemented in ORCA, in addition to the SARC/J auxiliary basis set,[74] to speed up all single-point and TDDFT calculations. DFT and COSX integration grids, and SCF convergence criteria were set to Grid6/finalgrid7, specialgridintacc (7, 7, 7), intaccx(4.34, 4.34, 4.67)/gridx(2, 2, 2), and tightscf. Both scalar-only and spin-orbit coupling corrected TDDFT were performed in all complexes to determine the extent of SOC between S_n and T_n states at the ground state equilibrium geometry. The first 30 S_n and T_n states were considered to cover the relevant region of the UV-Vis spectrum. TDDFT predicted spectra for all complexes were simulated using Multiwfn version 3.8, applying Gaussian broadening scheme with FWHM of 0.372 eV. We found a better agreement between experimental and simulated UV-Vis spectra with M06-2X, and thus most single point energies presented herein are calculated from this level of theory unless otherwise mentioned. Ground-state molecular orbital isosurfaces and electron-hole density maps for the relevant excited states were generated from Multiwfn with isosurface values of 0.04 and 0.002, respectively. Spin density maps for all relevant triplet states were simulated using Orca_plot module and Gabedit with isosurface value of 0.004. Photophysical parameters were obtained following a previously published protocol[31] as follows (Figure S20):

$$\Delta E^{\mathrm{phos}} = E(\mathrm{T}_{1,\mathrm{eq}}) - E(\mathrm{S}_0@\mathrm{T}_{1,\mathrm{eq}}) \tag{3}$$

$$\Delta E^{\mathrm{fluor}} = \mathrm{TD}(\mathrm{S}_{1,\mathrm{eq}}) - E(\mathrm{S}_0@\mathrm{S}_{1,\mathrm{eq}}) \tag{4}$$

$$\lambda^{\mathrm{ISC}}\ (\mathrm{S}_\mathrm{n}\rightarrow\mathrm{T}_1) = \mathrm{TD}(^1\mathrm{ILCT}) - E(\mathrm{T}_1) \tag{5}$$

$$\lambda^{\mathrm{IC}}\ (\mathrm{S}_\mathrm{n}\rightarrow\mathrm{S}_1) = \mathrm{TD}(^1\mathrm{ILCT}) - \mathrm{TD}(^1\mathrm{LLCT}) \tag{6}$$

$$\lambda^{\mathrm{T}} = E(\mathrm{S}_0@\mathrm{T}_{1,\mathrm{eq}}) - E(\mathrm{S}_0) \tag{7}$$

$$\lambda^{\mathrm{S}} = E(\mathrm{S}_0@\mathrm{S}_{1,\mathrm{eq}}) - E(\mathrm{S}_0) \tag{8}$$

The driving force of photoinduced symmetry-breaking charge separation was estimated using the Weller equation[58] as noted in the text (*vide supra*) for Zn($^{\mathbf{CF3}}\mathbf{L}$)$_2$, as this was the sole complex with an observable reduction event,

ASSOCIATED CONTENT

Supporting Information. Packing diagrams; additional UV-Vis absorption and emission spectra; computational data tables and figures; multi-nuclear NMR and HRMS spectra of all new compounds; crystallographic information files containing all X-ray data. CCDC 2119917-2119918 also contain the supplementary crystallographic data for this paper. The data can be obtained free of charge from The Cambridge Crystallographic Data Center via www.ccdc.cam.ac.uk/structures. The following files are available free of charge: Supporting Information File (PDF); Crystallographic Information Files (CIFs)

AUTHOR INFORMATION

Corresponding Authors

David E. Herbert (david.herbert@umanitoba.ca)

J.A. Gareth Williams (j.a.g.williams@durham.ac.uk)

ORCIDs

Issiah B. Lozada: 0000-0002-1689-2918

Jason D. Braun: 0000-0002-5850-8048

J. A. Gareth Williams: 0000-0002-4688-3000

David E. Herbert: 0000-0001-8190-2468

Author Contributions

The manuscript was written through contributions of all authors. All authors have given approval to the final version of the manuscript.

ACKNOWLEDGMENTS

The following sources of funding are gratefully acknowledged: the Natural Sciences Engineering Research Council of Canada for a Discovery Grant to DEH (RGPIN-2022-04501); the Canadian Foundation for Innovation and Research Manitoba for an award in support of an X-ray diffractometer (CFI #32146); Compute Canada for access to computational resources; and the University of Manitoba for the Bert & Lee Friesen Graduate Scholarship (IBL) and GETS support.

Gurleen Uppal and Prof. Johan van Lierop are graciously acknowledged for their assistance collecting PXRD data.

REFERENCES

(1) Wenger, O. S. Photoactive Complexes with Earth-Abundant Metals. *J. Am. Chem. Soc.* **2018**, *140*, 13522–13533.

(2) Wegeberg, C.; Wenger, O. S. Luminescent First-Row Transition Metal Complexes. *JACS Au* **2021**, *1*, 1860–1876.

(3) Hockin, B. M.; Li, C.; Robertson, N.; Zysman-Colman, E. Photoredox Catalysts Based on Earth-Abundant Metal Complexes. *Catal. Sci. Technol.* **2019**, *9*, 889–915.

(4) Kusaka, S.; Sakamoto, R.; Kitagawa, Y.; Okumura, M.; Nishihara, H. An Extremely Bright Heteroleptic Bis(Dipyrrinato)Zinc(II) Complex. *Chem. - Asian J.* **2012**, *7*, 907–910.

(5) Sakamoto, R.; Iwashima, T.; Kögel, J. F.; Kusaka, S.; Tsuchiya, M.; Kitagawa, Y.; Nishihara, H. Dissymmetric Bis(Dipyrrinato)Zinc(II) Complexes: Rich Variety and Bright Red to Near-Infrared Luminescence with a Large Pseudo-Stokes Shift. *J. Am. Chem. Soc.* **2016**, *138*, 5666–5677.

(6) Kögel, J. F.; Kusaka, S.; Sakamoto, R.; Iwashima, T.; Tsuchiya, M.; Toyoda, R.; Matsuoka, R.; Tsukamoto, T.; Yuasa, J.; Kitagawa, Y.; Kawai, T.; Nishihara, H. Heteroleptic [Bis(Oxazoline)](Dipyrrinato)Zinc(II) Complexes: Bright and Circularly Polarized Luminescence from an Originally Achiral Dipyrrinato Ligand. *Angew. Chem. Int. Ed.* **2016**, *55*, 1377–1381.

(7) Bestgen, S.; Schoo, C.; Neumeier, B. L.; Feuerstein, T. J.; Zovko, C.; Köppe, R.; Feldmann, C.; Roesky, P. W. Intensely Photoluminescent Diamidophosphines of the Alkaline-Earth Metals, Aluminum, and Zinc. *Angew. Chem. Int. Ed.* **2018**, *57*, 14265–14269.

(8) Dumur, F.; Beouch, L.; Tehfe, M.-A.; Contal, E.; Lepeltier, M.; Wantz, G.; Graff, B.; Goubard, F.; Mayer, C. R.; Lalevée, J.; Gigmes, D. Low-Cost Zinc Complexes for White Organic Light-Emitting Devices. *Thin Solid Films* **2014**, *564*, 351–360.

(9) Dumur, F. Zinc Complexes in OLEDs: An Overview. *Synth. Met.* **2014**, *195*, 241–251.

(10) Xie, Y.-Z.; Shan, G.-G.; Li, P.; Zhou, Z.-Y.; Su, Z.-M. A Novel Class of Zn(II) Schiff Base Complexes with Aggregation-Induced Emission Enhancement (AIEE) Properties: Synthesis, Characterization and Photophysical/Electrochemical Properties. *Dyes Pigm.* **2013**, *96*, 467–474.

(11) Bizzarri, C.; Spuling, E.; Knoll, D. M.; Volz, D.; Braese, S. Sustainable Metal Complexes for Organic Light-Emitting Diodes (OLEDs). *Coord. Chem. Rev.* **2018**, *373*, 49–82.

(12) Dua, S. K.; Rastogi, D. K.; Sahni, S. K. Four- and Six-Coordinate Zinc(II), Cadmium(II), and Mercury(II) Complexes of Terdentate Benzoyl Hydrazones. *J. Inorg. Nucl. Chem.* **1980**, *42*, 1711–1714.

(13) Ito, T.; Kato, M.; Ito, H. X-Ray Structural Study on Molecular Stereochemistries of Six-Coordinate Zinc(II) Complexes of Trans-ZnX_2N_4 Type. Out-of-Plane Displacement of Zinc(II) from a Plane Formed by in-Plane Four Nitrogens. *Bull. Chem. Soc. Jpn.* **1984**, *57*, 2634–2640.

(14) Lipton, A. S.; Wright, T. A.; Bowman, M. K.; Reger, D. L.; Ellis, P. D. Solid-State ^{67}Zn NMR Spectroscopy in Bioinorganic Chemistry. Spectra of Four- and Six-Coordinate Zinc Pyrazolylborate Complexes Obtained by Management of Proton Relaxation Rates with a Paramagnetic Dopant. *J. Am. Chem. Soc.* **2002**, *124*, 5850–5860.

(15) Klingele, J.; Steinfeld, G.; Klingele, M. H. Structural Characterisation of Mononuclear Zinc(II) Complexes of 4-Methyl-3,5-Di(2-Pyridyl)-4H-1,2,4-Triazole with Three-Atom Co-Ligands: $[Zn^{II}(Medpt)_2X]ClO_4$ (X = NCS^-, N_3^-, NO_2^-). *Trans. Met. Chem.* **2010**, *35*, 65–71.

(16) Shin, M. S.; Oh, B. J.; Ryu, J. Y.; Park, M. H.; Kim, M.; Lee, J.; Kim, Y. Synthesis, Characterization, and Cycloaddition Reaction Studies of Zinc(II) Acetate Complexes Containing 2,6-Bis(Pyrazol-1-Yl)Pyridine and 2,6-Bis(3,5-Dimethylpyrazol-1-Yl)Pyridine Ligands. *Polyhedron* **2017**, *125*, 101–106.

(17) Podjed, N.; Modec, B.; Alcaide, M. M.; Lopez-Serrano, J. From Cyclic Amines and Acetonitrile to Amidine Zinc(II) Complexes. *RSC Adv.* **2020**, *10*, 18200–18221.

(18) Chang, M.-C.; Otten, E. Synthesis and Ligand-Based Reduction Chemistry of Boron Difluoride Complexes with Redox-Active Formazanate Ligands. *Chem. Commun.* **2014**, *50*, 7431–7433.

(19) Braun, J. D.; Gray, P. A.; Sidhu, B. K.; Nemez, D. B.; Herbert, D. E. Zn-Templated Synthesis of Substituted (2,6-Diimine)Pyridine Proligands and Evaluation of Their Iron Complexes as Anolytes for Flow Battery Applications. *Dalton Trans.* **2020**, *49*, 16175–16183.

(20) Schauer, C. K.; Anderson, O. P.; Eaton, S. S.; Eaton, G. R. Crystal and Molecular Structure of a Six-Coordinate Zinc Porphyrin: Bis(Tetrahydrofuran)(5,10,15,20-Tetraphenylporphinato)Zinc(II). *Inorg. Chem.* **1985**, *24*, 4082–4086.

(21) Teo, T.-L.; Vetrichelvan, M.; Lai, Y.-H. Infinite Three-Dimensional Polymeric Metalloporphyrin Network via Six-Coordinate Zn(II) and Two Axial Oxygen Donors. *Org. Lett.* **2003**, *5*, 4207–4210.

(22) Favereau, L.; Cnossen, A.; Kelber, J. B.; Gong, J. Q.; Oetterli, R. M.; Cremers, J.; Herz, L. M.; Anderson, H. L. Six-Coordinate Zinc Porphyrins for Template-Directed Synthesis of Spiro-Fused Nanorings. *J. Am. Chem. Soc.* **2015**, *137*, 14256–14259.

(23) Martinez, S.; Igoa, F.; Carrera, I.; Seoane, G.; Veiga, N.; De Camargo, A. S. S.; Kremer, C.; Torres, J. A Zn(II) Luminescent Complex with a Schiff Base Ligand: Solution, Computational and Solid State Studies. *J. Coord. Chem.* **2018**, *71*, 874–889.

(24) Mrózek, O.; Gernert, M.; Belyaev, A.; Mitra, M.; Janiak, L.; Marian, C. M.; Steffen, A. Ultra-Long Lived Luminescent Triplet Excited States in Cyclic (Alkyl)(Amino)Carbene Complexes of Zn(II) Halides. *Chem. - Eur. J.* **2022**, e202201114.

(25) Temerova, D.; Kisel, K. S.; Eskelinen, T.; Melnikov, A. S.; Kinnunen, N.; Hirva, P.; Shakirova, J. R.; Tunik, S. P.; Grachova, E. V.; Koshevoy, I. O. Diversifying the Luminescence of Phenanthro-Diimine Ligands in Zinc Complexes. *Inorg. Chem. Front.* **2021**, *8*, 2549–2560.

(26) Yang, X.-G.; Zhai, Z.-M.; Lu, X.-M.; Qin, J.-H.; Li, F.-F.; Ma, L.-F. Hexanuclear Zn(II)-Induced Dense π-Stacking in a Metal–Organic Framework Featuring Long-Lasting Room Temperature Phosphorescence. *Inorg. Chem.* **2020**, *59*, 10395–10399.

(27) Li, D.; Yang, X.; Yan, D. Cluster-Based Metal–Organic Frameworks: Modulated Singlet–Triplet Excited States and Temperature-Responsive Phosphorescent Switch. *ACS Appl. Mater. Interf.* **2018**, *10*, 34377–34384.

(28) Kobayashi, F.; Ohtani, R.; Teraoka, S.; Yoshida, M.; Kato, M.; Zhang, Y.; Lindoy, L. F.; Hayami, S.; Nakamura, M. Phosphorescence at Low Temperature by External Heavy-Atom Effect in Zinc(II) Clusters. *Chem. - Eur. J.* **2019**, *25*, 5875–5879.

(29) Mondal, R.; Giesbrecht, P. K.; Herbert, D. E. Nickel(II), Copper(I) and Zinc(II) Complexes Supported by a (4-Diphenylphosphino)Phenanthridine Ligand. *Polyhedron* **2016**, *108*, 156–162.

(30) Mandapati, P.; Giesbrecht, P. K.; Davis, R. L.; Herbert, D. E. Phenanthridine-Containing Pincer-like Amido Complexes of Nickel, Palladium, and Platinum. *Inorg. Chem.* **2017**, *56*, 3674–3685.

(31) Mondal, R.; Lozada, I. B.; Davis, R. L.; Williams, J. A. G.; Herbert, D. E. Site-Selective Benzannulation of N-Heterocycles in Bidentate Ligands Leads to Blue-Shifted Emission from [(*P^N*)Cu]$_2$(μ-X)$_2$ Dimers. *Inorg. Chem.* **2018**, *57*, 4966–4978.

(32) Mondal, R.; Lozada, I. B.; Davis, R. L.; Williams, J. A. G.; Herbert, D. E. Exploiting Synergy between Ligand Design and Counterion Interactions to Boost Room Temperature Phosphorescence from Cu(I) Compounds. *J. Mater. Chem. C* **2019**, *7*, 3772–3778.

(33) Mandapati, P.; Braun, J. D.; Killeen, C.; Davis, R. L.; Williams, J. A. G.; Herbert, D. E. Luminescent Platinum(II) Complexes of N^N$^-$^N Amido Ligands with Benzannulated N-Heterocyclic Donor Arms: Quinolines Offer Unexpectedly Deeper Red Phosphorescence than Phenanthridines. *Inorg. Chem.* **2019**, *58*, 14808–14817.

(34) Mandapati, P.; Braun, J. D.; Lozada, I. B.; Williams, J. A. G.; Herbert, D. E. Deep-Red Luminescence from Platinum(II) Complexes of N^N$^-$^N-Amido Ligands with Benzannulated N-Heterocyclic Donor Arms. *Inorg. Chem.* **2020**, *59*, 12504–12517.

(35) Braun, J. D.; Lozada, I. B.; Kolodziej, C.; Burda, C.; Newman, K. M. E.; van Lierop, J.; Davis, R. L.; Herbert, D. E. Iron(II) Coordination Complexes with Panchromatic Absorption and Nanosecond Charge-Transfer Excited State Lifetimes. *Nat. Chem.* **2019**, *11*, 1144–1150.

(36) Lozada, I. B.; Huang, B.; Stilgenbauer, M.; Beach, T.; Qiu, Z.; Zheng, Y.; Herbert, D. E. Monofunctional Platinum(II) Anticancer Complexes Based on Multidentate Phenanthridine-Containing Ligand Frameworks. *Dalton Trans.* **2020**, *49*, 6557–6560.

(37) Lozada, I. B.; Williams, J. A. G.; Herbert, D. E. Platinum(II) Complexes of Benzannulated N^N$^-$^O-Amido Ligands: Bright Orange Phosphors with Long-Lived Excited States. *Inorg. Chem. Front.* **2022**, *9*, 10–22.

(38) Lozada, I. B.; Ortiz, R. J.; Braun, J. D.; Williams, J. A. G.; Herbert, D. E. Donor–Acceptor Boron-Ketoiminate Complexes with Pendent N-Heterocyclic Arms: Switched-on Luminescence through N-Heterocycle Methylation. *J. Org. Chem.* **2022**, *87*, 184–196.

(39) Lozada, I. B.; Murray, T.; Herbert, D. E. Monomeric Zinc(II) Amide Complexes Supported by Bidentate, Benzannulated Phenanthridine Amido Ligands. *Polyhedron* **2019**, *161*, 261–267.

(40) Bridgeman, A. J.; Cavigliasso, G.; Ireland, L. R.; Rothery, J. The Mayer Bond Order as a Tool in Inorganic Chemistry. *J. Chem. Soc., Dalton Trans.* **2001**, 2095–2108.

(41) Lu, T.; Chen, F. Atomic Dipole Moment Corrected Hirshfeld Population Method. *J. Theor. Comput. Chem.* **2012**, *11*, 163–183.

(42) Donckt, E. V.; Dramaix, R.; Nasielski, J.; Vogels, C. Photochemistry of Aromatic Compounds. Part 1.—Acid-Base Properties of Singlet and Triplet Excited States of Pyrene Derivatives and Aza-Aromatic Compounds. *Trans. Faraday Soc.* **1969**, *65*, 3258–3262.

(43) Zander, M. The Significance of Donor-Acceptor Interactions in the External Heavy Atom Effect of Silver Nitrate on the Luminescence Behavior of Aza-Aromatic Systems and Carbazoles. *Z. Naturforsch. A* **1978**, *33*, 998–1000.

(44) Norek, M.; Dresner, J.; Prochorow, J. Spectroscopy and Photophysics of Monoazaphenanthrenes. I. Absorption and Fluorescence Spectra of Phenanthridine and 7,8-Benzoquinoline. *Acta Phys. Pol., A* **2003**, *104*, 425–439.

(45) Oyler, K. D.; Coughlin, F. J.; Bernhard, S. Controlling the Helicity of 2,2‘-Bipyridyl Ruthenium(II) and Zinc(II) Hemicage Complexes. *J. Am. Chem. Soc.* **2007**, *129*, 210–217.

(46) Mei, J.; Leung, N. L. C.; Kwok, R. T. K.; Lam, J. W. Y.; Tang, B. Z. Aggregation-Induced Emission: Together We Shine, United We Soar! *Chem. Rev.* **2015**, *115*, 11718–11940.

(47) Singh, K.; Siddiqui, I.; Sridharan, V.; Kumar Yadav, R. A.; Jou, J.-H.; Adhikari, D. Aggregation-Induced Enhanced Emission-Active Zinc(II) β-Diketiminate Complexes Enabling High-Performance Solution-Processable OLEDs. *Inorg. Chem.* **2021**, *60*, 19128–19135.

(48) Singh, K.; S., V.; Adhikari, D. Visible Light Photoredox by a (Ph,ArNacNac)2Zn Photocatalyst: Photophysical Properties and Mechanistic Understanding. *Inorg. Chem. Front.* **2021**, *8*, 2078–2087.

(49) Montalti, M.; Credi, A.; Prodi, L.; Gandolfi, M. *Handbook of Photochemistry. 3rd Ed.*; CRC Press: Boca Raton, 2006.

(50) Larsen, C. B.; Braun, J. D.; Lozada, I. B.; Kunnus, K.; Biasin, E.; Kolodziej, C.; Burda, C.; Cordones, A. A.; Gaffney, K. J.; Herbert, D. E. Reduction of Electron Repulsion in Highly Covalent Fe-Amido Complexes Counteracts the Impact of a Weak Ligand Field on Excited-State Ordering. *J. Am. Chem. Soc.* **2021**, *143*, 20645–20656.

(51) Caspar, J. V.; Meyer, T. J. Photochemistry of Tris(2,2’-Bipyridine)Ruthenium(2+) Ion ($Ru(Bpy)_3^{2+}$). Solvent Effects. *J. Am. Chem. Soc.* **1983**, *105*, 5583–5590.

(52) Das, S.; Thornbury, W. G.; Bartynski, A. N.; Thompson, M. E.; Bradforth, S. E. Manipulating Triplet Yield through Control of Symmetry-Breaking Charge Transfer. *J. Phys. Chem. Lett.* **2018**, *9*, 3264–3270.

(53) Trinh, C.; Kirlikovali, K.; Das, S.; Ener, M. E.; Gray, H. B.; Djurovich, P.; Bradforth, S. E.; Thompson, M. E. Symmetry-Breaking Charge Transfer of Visible Light Absorbing Systems: Zinc Dipyrrins. *J. Phys. Chem. C* **2014**, *118*, 21834–21845.

(54) Kellogg, M.; Akil, A.; Muthiah Ravinson, D. S.; Estergreen, L.; Bradforth, S. E.; Thompson, M. E. Symmetry Breaking Charge Transfer as a Means to Study Electron Transfer with No Driving Force. *Faraday Discuss.* **2019**, *216*, 379–394.

(55) Mahmood, Z.; Rehmat, N.; Ji, S.; Zhao, J.; Sun, S.; Di Donato, M.; Li, M.; Teddei, M.; Huo, Y. Tuning the Triplet Excited State of Bis(Dipyrrin) Zinc(II) Complexes: Symmetry Breaking Charge Transfer Architecture with Exceptionally Long Lived Triplet State for Upconversion. *Chem. Eur. J.* **2020**, *26*, 14912–14918.

(56) Weller, A. Photoinduced Electron Transfer in Solution: Exciplex and Radical Ion Pair Formation Free Enthalpies and Their Solvent Dependence By. *Z. Phys. Chem.* **1982**, *133*, 93–98.

(57) Rehm, D.; Weller, A. Kinetics of Fluorescence Quenching by Electron and H-Atom Transfer. *Isr. J. Chem.* **1970**, *8*, 259–271.

(58) Vauthey, E. Photoinduced Symmetry-Breaking Charge Separation. *ChemPhysChem* **2012**, *13*, 2001–2011.

(59) Bruker-AXS. APEX3 V2016.1-0, 2016.

(60) Dolomanov, O. V.; Bourhis, L. J.; Gildea, R. J.; Howard, J. A. K.; Puschmann, H. OLEX2: A Complete Structure Solution, Refinement and Analysis Program. *J. Appl. Crystallogr.* **2009**, *42*, 339–341.

(61) Spek, A. L. Structure Validation in Chemical Crystallography. *Acta Cryst.* **2009**, *D65*, 148–155.

(62) Neese, F. The ORCA Program System. *WIREs Comp. Mol. Sci.* **2012**, *2*, 73–78.

(63) Neese, F. Software Update: The ORCA Program System, Version 4.0. *WIREs Comp. Mol. Sci.* **2018**, *8*, e1327.

(64) Becke, A. D. Density-functional Thermochemistry. III. The Role of Exact Exchange. *J. Chem. Phys.* **1998**, *98*, 5648.

(65) Lee, C.; Yang, W.; Parr, R. G. Development of the Colle-Salvetti Correlation-Energy Formula into a Functional of the Electron Density. *Phys. Rev. B* **1988**, *37*, 785–789.

(66) Vosko, S. H.; Wilk, L.; Nusair, M. Accurate Spin-Dependent Electron Liquid Correlation Energies for Local Spin Density Calculations: A Critical Analysis. *Can. J. Phys.* **1980**, *58*, 1200–1211.